

©2001 Society of Photo-Optical Instrumentation Engineers (SPIE). One print or electronic copy may be made for personal use only. Systematic reproduction and distribution, duplication of any material in this paper for a fee or for commercial purposes, or modification of the content of the paper are prohibited.

Du, Qian, and Chein-I. Chang. "Hidden Markov Model Approach to Spectral Analysis for Hyperspectral Imagery." *Optical Engineering* 40, no. 10 (October 2001): 2277–84. <https://doi.org/10.1117/1.1404430>.
<https://doi.org/10.1117/1.1404430>

Access to this work was provided by the University of Maryland, Baltimore County (UMBC) ScholarWorks@UMBC digital repository on the Maryland Shared Open Access (MD-SOAR) platform.

Please provide feedback

Please support the ScholarWorks@UMBC repository by emailing scholarworks-group@umbc.edu and telling us what having access to this work means to you and why it's important to you. Thank you.

Hidden Markov model approach to spectral analysis for hyperspectral imagery

Qian Du, MEMBER SPIE

Texas A&M University-Kingsville
Department of Electrical Engineering and
Computer Science
Kingsville, TX 78363

Chein-I Chang, MEMBER SPIE

University of Maryland Baltimore County
Department of Computer Science
and Electrical Engineering
Remote Sensing Signal and Image
Processing Laboratory
1000 Hilltop Circle
Baltimore, MD 21250

Abstract. The hidden Markov model (HMM) has been widely used in speech recognition where it models a speech signal as a doubly stochastic process with a hidden state process that can be observed only through a sequence of observations. We present a new application of the HMM in hyperspectral image analysis inspired by the analogy between the temporal variability of a speech signal and the spectral variability of a remote sensing image pixel vector. The idea is to model a hyperspectral spectral vector as a stochastic process where the spectral correlation and band-to-band variability are modeled by a hidden Markov process with parameters determined by the spectrum of the vector that forms a sequence of observations. With this interpretation, a new HMM-based spectral measure, referred to as the HMM information divergence (HMMID), is derived to characterize spectral properties. To evaluate the performance of this new measure, it is further compared to two commonly used spectral measures, Euclidean distance (ED) and the spectral angle mapper (SAM), and the recently proposed spectral information divergence (SID). The experimental results show that the HMMID performs better than the other three measures in characterizing spectral information at the expense of computational complexity. © 2001 Society of Photo-Optical Instrumentation Engineers. [DOI: 10.1117/1.1404430]

Subject terms: Euclidean distance; hidden Markov model; hidden Markov model information divergence; hyperspectral images; spectral angle mapper; spectral characterization; spectral information divergence.

Paper 990515 received Dec. 27, 1999; revised manuscript received Apr. 17, 2001; accepted for publication Apr. 27, 2001.

1 Introduction

The advent of recent remote sensing instruments has significantly improved capability of ground-based data collection in many fields such as agriculture, geology, geography, law enforcement, defense, etc.¹ For example, two hyperspectral sensors, 224-band AVIRIS (airborne visible/infrared imaging spectrometer) and 210-band HYDICE (hyperspectral digital imagery collection experiment), that are currently being used and operated in an airborne platform implement hundreds of spectral channels to uncover many material substances that generally are resolved by multispectral sensors with difficulty. Since a scene pixel is usually represented by a column vector, where each component contains specific spectral information provided by one particular channel, the more channels are used, the more spectral information is available. As a result, a hyperspectral image pixel vector possesses much richer spectral information than does a multispectral image pixel vector and may also have subtle information that a multispectral image pixel vector may not have.

However, due to noise and atmospheric effects, a material substance, referred to as the endmember,² may be represented by different spectral signatures from pixel to pixel during data acquisition and varies with different degrees of its mixture with background signatures. To account for such spectral variability, an information theoretic criterion-based hyperspectral measure, spectral information divergence

(SID), was recently developed³ and has shown some success in spectral characterization. It models the spectrum of a hyperspectral image pixel vector as a random variable to capture the stochastic behaviors of the pixel vector. The similarity between two pixel vectors is then measured by the SID. The results were compared to several commonly used metrics, such as Euclidean distance⁴ (ED) and spectral angle mapper² (SAM), and were shown to be more effective than ED and SAM in the sense of capturing the spectral similarity and variability.³

In this paper, we present another statistical approach that makes use of a hidden Markov model (HMM) to characterize the unobserved and hidden spectral properties of a hyperspectral image pixel vector. The HMM has been widely used in speech recognition⁵⁻⁷ to model a speech signal as a doubly stochastic process with a hidden state process that can be observed only through a sequence of observations. Since the temporal variability of a speech signal is similar to the spectral variability of a remote sensing image pixel vector, the same idea can be applied to a hyperspectral spectral vector. It makes use of a hidden Markov process to characterize the spectral correlation and band-to-band variability where the model parameters are determined by the spectrum of the pixel vector that forms an observation sequence. In speech processing, the same word spoken in different times generally results in different speech signals such as pitches. This is also true for the case that the spectrum of the same endmember varies from pixel to pixel

because it may be mixed with various endmembers such as background or natural object signatures. Using the HMM as an underlying process that describes the unobserved spectral properties, a new HMM-based spectral measure, referred to as the HMM information divergence (HMMID), is derived for spectral characterization. Because the HMM has been successfully applied to speech recognition, the HMMID may also provide new insight into spectral analysis of hyperspectral imagery.

To evaluate the performance of the HMMID, the ED, the SAM and the SID are used for comparison. The ED and the SAM capture the geometric difference between the spectra of two pixel vectors and there is no probabilistic description involved in these measures. Therefore, the ED and the SAM can be viewed as deterministic spectral metrics. By contrast, the SID and the HMMID are stochastic measures that introduce the concept of probability to describe the spectral band-to-band correlation. Compared to the SID, which models a hyperspectral image pixel vector as a random variable, the HMMID assumes that each pixel can be characterized by an HMM with the hidden state process estimated from its spectrum. The resulting HMM is then used to describe the unobserved spectral properties. A similar approach was also found in a Kalman filtering-based linear unmixing method that used a state equation to describe the interpixel correlation.^{8,9} Consequently, the HMM complexity should provide a better capability than the SID in capturing spectral variability. As we show in the experiments, this is indeed the case.

The remainder of this paper is organized as follows. Section 2 briefly describes the HMM. Section 3 presents a new HMM-based hyperspectral similarity measure, HMMID, for spectral similarity. Section 4 introduces two criteria for spectral discriminability.³ Section 5 conducts experiments to demonstrate the performance of the HMMID relative to the SID, the ED and the SAM. Section 6 concludes with brief remarks.

2 HMM

Let $\mathbf{o}=(o_1 o_2 \dots o_T)$ be an observation process with o_t being the observation taken place at time t and T is the number of observations made in the process. Assume that there are N states denoted by $\{1, 2, \dots, N\}$ and the state at time t is denoted by q_t . Let $\mathbf{A}=\{a_{ij}\}_{1 \leq i, j \leq N}$ be the state transition matrix with a_{ij} given by

$$a_{ij}=P(q_{t+1}=j|q_t=i), \quad (1)$$

and $\mathbf{B}=[b_j(o_t)]_{1 \leq j \leq N, 1 \leq t \leq T}$ be the observation probability density matrix, where $b_j(o_t)$ is the probability density of the observation o_t at time t in the j 'th state. We further assume that $\boldsymbol{\pi}=(\pi_1 \pi_2 \dots \pi_N)$ is the initial state distribution with π_j given by

$$\pi_j=P(q_1=j). \quad (2)$$

Thus, an HMM can be uniquely defined by a parameter triplet, denoted by $\lambda=(\mathbf{A}, \mathbf{B}, \boldsymbol{\pi})$, which can be estimated by the Baum-Welch algorithm using the maximum likelihood estimation as follows.⁵

Assume that the probability density $b_j(o_t)$ is a Gaussian mixture. It was shown in Ref. 6 that it is equivalent to a multistage single Gaussian density given by

$$b_j(o_t)=\frac{1}{[2\pi\sigma_j^2]^{1/2}}\exp\left[-\frac{(o_t-\mu_j)^2}{2\sigma_j^2}\right], \quad (3)$$

where μ_j and σ_j^2 are the mean and variance of the observation o_t in the j 'th state, respectively.

Now we define the forward probability $\alpha_j(t)$ as the joint probability of observing the first t observations o_1, o_2, \dots, o_t in the j 'th state at time t . It can be solved by

$$\alpha_j(1)=\pi_j b_j(o_1), \quad (4)$$

$$\alpha_j(t)=\left[\sum_{i=1}^N \alpha_i(t-1)a_{ij}\right]b_j(o_t) \text{ for } 1 < t \leq T. \quad (5)$$

Similarly, we define the backward probability $\beta_j(t)$ as the conditional probability of observing the observations $o_{t+1}, o_{t+2}, \dots, o_T$ given that the state at time t is j . It can be solved by

$$\beta_j(T)=1, \quad (6)$$

$$\beta_j(t)=\sum_{i=1}^N a_{ji}b_i(o_{t+1})\beta_i(t+1) \text{ for } 1 < t \leq T. \quad (7)$$

Let $\gamma_j(t)$ denote the conditional probability of $b_j(o_t)$ given the observation $\mathbf{o}=(o_1 o_2 \dots o_T)$ and $\xi_{ij}(t)$ denote the conditional probability of a transition from state i to state j at time $t+1$ given the observation $\mathbf{o}=(o_1 o_2 \dots o_T)$. Then they can be calculated as follows

$$\gamma_j(t)=\frac{\alpha_j(t)\beta_j(t)}{\sum_{i=1}^N \alpha_i(t)\beta_i(t)}, \quad (8)$$

$$\xi_{ij}(t)=\frac{\alpha_i(t)a_{ij}b_j(o_{t+1})\beta_j(t+1)}{\sum_{k=1}^N \alpha_i(t)a_{ik}b_k(o_{t+1})\beta_k(t+1)}. \quad (9)$$

Using Eqs. (8) and (9), the μ_j , σ_j^2 , a_{ij} and π_j can be estimated by the following equations

$$\hat{\mu}_j(t)=\frac{\sum_{t=1}^T [\gamma_j(t)o_t]}{\sum_{t=1}^T \gamma_j(t)}, \quad (10)$$

$$\hat{\sigma}_j^2(t)=\frac{\sum_{t=1}^T [\gamma_j(t)(o_t-\hat{\mu}_j(t))^2]}{\sum_{t=1}^T \gamma_j(t)}, \quad (11)$$

$$\hat{a}_{ij}(t)=\frac{\sum_{t=1}^{T-1} \xi_{ij}(t)}{\sum_{t=1}^{T-1} \gamma_i(t)}, \quad (12)$$

$$\hat{\pi}_j=\gamma_j(1). \quad (13)$$

3 HMM-Based Hyperspectral Measure

As indicated previously, an endmember can be represented by variants of its true spectral signature from pixel to pixel

because of unpredicted mixing occurring in a pixel vector. However, we must have some unobserved properties governed by this particular endmember that can distinguish it from other endmembers. This spectral characterization is very similar to speech signals where one of the key features is pitch. If we assume the observation sequence $\mathbf{o} = (o_1 o_2 \dots o_T)$ is represented by the spectral signature \mathbf{s}_i of the i 'th sample pixel vector \mathbf{r}_i in a hyperspectral image, we can use the HMM to capture the unobserved and hidden spectral properties of \mathbf{s}_i . Let $\lambda_{\mathbf{s}_i}$ be the parameter vector used to specify \mathbf{s}_i and let $\text{HMM}(\lambda_{\mathbf{s}_i})$ be the HMM determined by $\lambda_{\mathbf{s}_i}$. Then we can define the self information of \mathbf{s}_i provided by $\text{HMM}(\lambda_{\mathbf{s}_i})$, denoted by $I_{\text{HMM}(\lambda_{\mathbf{s}_i})}(\mathbf{s}_i)$ as follows

$$I_{\text{HMM}(\lambda_{\mathbf{s}_i})}(\mathbf{s}_i) = -\frac{1}{T} [\log P(\mathbf{s}_i | \lambda_{\mathbf{s}_i})]. \quad (14)$$

Assume that there is another HMM, denoted by $\text{HMM}(\lambda)$ to model \mathbf{s}_i . The discrepancy between $\text{HMM}(\lambda)$ and $\text{HMM}(\lambda_{\mathbf{s}_i})$ can be expressed by

$$J_{\text{HMM}(\lambda_{\mathbf{s}_i}; \lambda) = I_{\text{HMM}(\lambda_{\mathbf{s}_i})}(\mathbf{s}_i) - I_{\text{HMM}(\lambda)}(\mathbf{s}_i) \\ = \frac{1}{T} [\log P(\mathbf{s}_i | \lambda) - \log P(\mathbf{s}_i | \lambda_{\mathbf{s}_i})] \quad (15)$$

which is generally referred to as the entropy of $\text{HMM}(\lambda)$ relative to $\text{HMM}(\lambda_{\mathbf{s}_i})$ and also known as the Kullback-Leibler information distance, cross entropy or directed divergence.¹⁰ Suppose that we are given two hyperspectral image pixels \mathbf{r}_i and \mathbf{r}_j with their spectral signatures given by $\mathbf{s}_i = (s_{i1}, \dots, s_{iL})^T$ and $\mathbf{s}_j = (s_{j1}, \dots, s_{jL})^T$, respectively, where L is the total number of spectral bands. We can further define an information distance between their associated HMMs, $\text{HMM}(\lambda_{\mathbf{s}_i})$ and $\text{HMM}(\lambda_{\mathbf{s}_j})$, called HMMID, by

$$\text{HMMID}(\lambda_{\mathbf{s}_i}, \lambda_{\mathbf{s}_j}) = J_{\text{HMM}(\lambda_{\mathbf{s}_i}, \lambda_{\mathbf{s}_j})} + J_{\text{HMM}(\lambda_{\mathbf{s}_j}, \lambda_{\mathbf{s}_i})}. \quad (16)$$

A similar hyperspectral measure, referred to as SID was also based on Kullback-Leibler information distance.³ Instead of using HMM, as proposed, the SID normalized the spectral signature $\mathbf{s}_i = (s_{i1}, \dots, s_{iL})^T$ of a pixel \mathbf{r}_i to unity and considered it as a probability distribution of the pixel vector \mathbf{r}_i . In this case, we can define a probability vector, $\mathbf{p}_i = (p_{i1}, \dots, p_{iL})^T$ resulting from \mathbf{s}_i by

$$p_{il} = \frac{s_{il}}{\sum_{k=1}^L s_{ik}}. \quad (17)$$

Similarly, we can also find a probability vector of \mathbf{r}_j , $\mathbf{p}_j = (p_{j1}, \dots, p_{jL})^T$ using its spectral signature $\mathbf{s}_j = (s_{j1}, \dots, s_{jL})^T$ with

$$p_{jl} = \frac{s_{jl}}{\sum_{k=1}^L s_{jk}}. \quad (18)$$

Now we can use Kullback-Leibler information distance to define SID between two pixel vectors \mathbf{r}_i and \mathbf{r}_j with their respective spectral signatures $\mathbf{s}_i = (s_{i1}, \dots, s_{iL})^T$ and $\mathbf{s}_j = (s_{j1}, \dots, s_{jL})^T$ by

$$\text{SID}(\mathbf{p}_i, \mathbf{p}_j) = D(\mathbf{p}_i \| \mathbf{p}_j) = \sum_{l=1}^L p_{il} \log \frac{p_{il}}{p_{jl}} + \sum_{l=1}^L p_{jl} \log \frac{p_{jl}}{p_{il}}. \quad (19)$$

To conduct a comparative analysis, two other popular similarity measures, ED and SAM (defined next), are used for the experiments in Section 5 to evaluate performance of HMMID and SID.

$$\text{ED}(\mathbf{s}_i, \mathbf{s}_j) = \|\mathbf{s}_i - \mathbf{s}_j\| = \left[\sum_{l=1}^L (s_{il} - s_{jl})^2 \right]^{1/2}, \quad (20)$$

$$\text{SAM}(\mathbf{s}_i, \mathbf{s}_j) = \cos^{-1} \left(\frac{\mathbf{s}_i \cdot \mathbf{s}_j}{\|\mathbf{s}_i\| \|\mathbf{s}_j\|} \right) \\ \equiv \cos^{-1} \left[\frac{\sum_{l=1}^L s_{il} s_{jl}}{(\sum_{l=1}^L s_{il}^2)^{1/2} (\sum_{l=1}^L s_{jl}^2)^{1/2}} \right] \quad (\text{in radians}). \quad (21)$$

Note that if both \mathbf{s}_i and \mathbf{s}_j are normalized to unity, the relationship between the $\text{ED}(\mathbf{s}_i, \mathbf{s}_j)$ and the $\text{SAM}(\mathbf{s}_i, \mathbf{s}_j)$ can be established as follows.

$$\text{ED}(\mathbf{s}_i, \mathbf{s}_j) = (2 - 2\langle \mathbf{s}_i, \mathbf{s}_j \rangle)^{1/2} \\ = (2\{1 - \cos[\text{SAM}(\mathbf{s}_i, \mathbf{s}_j)]\})^{1/2} \\ = 2 \left\{ \frac{1 - \cos[\text{SAM}(\mathbf{s}_i, \mathbf{s}_j)]}{2} \right\}^{1/2} \\ = 2 \sin \left[\frac{\text{SAM}(\mathbf{s}_i, \mathbf{s}_j)}{2} \right], \quad (22)$$

where $\langle \mathbf{s}_i, \mathbf{s}_j \rangle = \sum_{l=1}^L s_{il} s_{jl}$. When the $\text{SAM}(\mathbf{s}_i, \mathbf{s}_j)$ is small, $2 \sin[\text{SAM}(\mathbf{s}_i, \mathbf{s}_j)/2] \approx \text{SAM}(\mathbf{s}_i, \mathbf{s}_j)$. In this case, the $\text{SAM}(\mathbf{s}_i, \mathbf{s}_j)$ is nearly the same as the $\text{ED}(\mathbf{s}_i, \mathbf{s}_j)$. This is demonstrated in the AVIRIS experiments.

4 Spectral Discriminatory Criteria

In the previous section, the ED, the SAM, the SID and the HMMID, given by Eqs. (16) and (19)–(21), were developed to measure the similarity between the spectra of two pixels. However, it seems that there is no criteria available in the literature to evaluate two given spectral similarity measures. In this section, we describe two spectral discriminatory criteria that may be useful for performance analysis.³

4.1 Relative Spectral Discriminatory Probability

In many applications, it is often the case that we are required to identify a target pixel of interest, say \mathbf{t} from an unknown image scene using an existing spectral library or database Δ . Under such a circumstance, it is interesting to calculate the likelihood of \mathbf{t} to be identified by signatures in

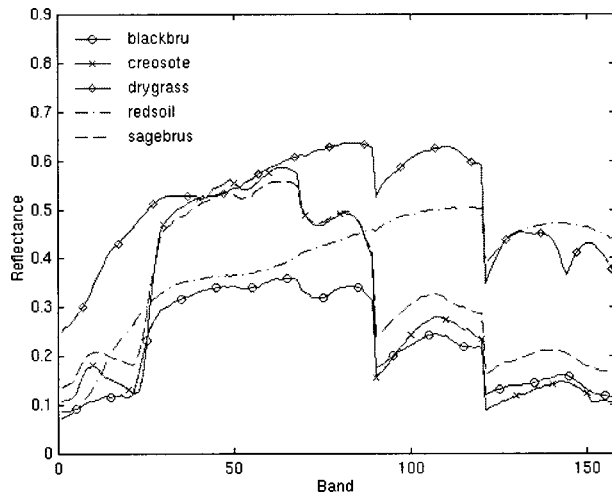


Fig. 1 Spectra of the five AVIRIS signatures: blackbrush, creosote leaves, dry grass, red soil and sagebrush.

the Δ . Specifically, let $\{s_j\}_{j=1}^J$ be J spectral signatures in the Δ . We first calculate the spectral discriminatory probabilities of all s_j 's in Δ relative to \mathbf{t} as follows.

$$p_{\mathbf{t},\Delta}^m(i) = \frac{m(\mathbf{t}, s_i)}{\sum_{j=1}^J m(\mathbf{t}, s_j)} \quad \text{for } i = 1, 2, \dots, J, \quad (23)$$

where $\sum_{j=1}^J m(\mathbf{t}, s_j)$ is a normalization constant determined by \mathbf{t} and Δ . The resulting probability vector $\mathbf{p}_{\mathbf{t},\Delta}^m = [p_{\mathbf{t},\Delta}^m(1), p_{\mathbf{t},\Delta}^m(2), \dots, p_{\mathbf{t},\Delta}^m(J)]^T$ is defined to be relative spectral discriminatory probability (RSDPB) of Δ with respect to \mathbf{t} using $m(\cdot, \cdot)$ or spectral discriminatory probability vector of Δ with respect to \mathbf{t} using $m(\cdot, \cdot)$. Using Eq. (23) we can identify \mathbf{t} via Δ by selecting the one with the smallest relative spectral discriminability probability.

4.2 Relative Spectral Discriminatory Entropy

Since $\mathbf{p}_{\mathbf{t},\Delta}^m = [p_{\mathbf{t},\Delta}^m(1), p_{\mathbf{t},\Delta}^m(2), \dots, p_{\mathbf{t},\Delta}^m(J)]^T$, given by Eq. (23), is the relative spectral discriminability probability vector of \mathbf{t} using a designated set of spectral signatures, $\Delta = \{s_j\}_{j=1}^J$, we can further define the relative spectral discriminatory entropy (RSDE) of Δ with respect to the spectral signature \mathbf{t} using $m(\cdot, \cdot)$ denoted by $H_{\text{RSDE}}^m(\mathbf{t}; \Delta)$ as follows.

$$H_{\text{RSDE}}^m(\mathbf{t}; \Delta) = - \sum_{j=1}^J p_{\mathbf{t},\Delta}^m(j) \log p_{\mathbf{t},\Delta}^m(j). \quad (24)$$

Equation (24) provides an uncertainty measure of identifying \mathbf{t} using any spectral signature from a data base or library $\Delta = \{s_j\}_{j=1}^J$. The smaller the $H_{\text{RSDE}}^m(\mathbf{t}; \Delta)$, the less the uncertainty of identifying \mathbf{t} using Δ .

5 Experiments

Two data sets were used for experiments to evaluate the performance of the HMMID. The first data set was a set of AVIRIS laboratory data and the second data set was obtained from a HYDICE image scene.

Table 1 Spectral similarity produced by ED among the five AVIRIS data in Fig. 1.

	Blackbrush	Creosote	Drygrass	Redsoil	Sagebrush
Blackbrush	0	0.1765	0.2568	0.4031	0.0681
Creosote		0	0.4182	0.5637	0.1288
Drygrass			0	0.2175	0.2957
Redsoil				0	0.4477
Sagebrush					0

5.1 Example 1: AVIRIS Data

The data used in the following example are the same AVIRIS reflectance data considered in Refs. 11 and 12. They were five field reflectance spectra, blackbrush (indicated by an open circle), creosote leaves (indicated by an asterisk), dry grass (indicated by a diamond), red soil (indicated by a dash-dotted line) and sagebrush (indicated by a dashed line) shown in Fig. 1 with spectral coverage from 0.4 to 2.5 μm . There were 158 bands after water bands were removed and all spectra were normalized to unity. From Fig. 1, we can see that the spectra among blackbrush, creosote leaves and sagebrush are very similar. However, a rigorous measure of closeness between five signatures is very difficult to estimate by visual inspection. Tables 1–4 tabulate the spectral similarity among these five signatures using the ED, the SAM, the SID and the HMMID, respectively. The smaller the value is between two signatures, the more similar are the two signatures. The results produced by the ED and the SAM were nearly the same as shown by Eq. (22). According to these tables, blackbrush is closest to sagebrush, while the creosote leaves are closest to sagebrush. If we examine the last column under sagebrush in Tables 1–4, we find that sagebrush is closer to blackbrush than to creosote leaves. The similarity values produced by the ED and the SAM between blackbrush and sagebrush were about twice as much as between creosote leaves and sagebrush. The similarity values produced by the SID between blackbrush and sagebrush were about five times as much as between creosote leaves and sagebrush. The similarity values produced by the HMMID between blackbrush and sagebrush were about six times as much as between creosote leaves and sagebrush. For signatures whose spectra are dissimilar, the HMMID produced even much greater values than did other three measures. For example, the similarity values between red soil and blackbrush, between red soil and creosote leaves, and between red soil and sagebrush were 3.9182, 6.7333 and 3.4166, respectively, com-

Table 2 Spectral similarity produced by SAM among the five AVIRIS data in Fig. 1.

	Blackbrush	Creosote	Drygrass	Redsoil	Sagebrush
Blackbrush	0	0.1767	0.2575	0.4058	0.0681
Creosote		0	0.4213	0.5714	0.1289
Drygrass			0	0.2179	0.2968
Redsoil				0	0.4515
Sagebrush					0

Table 3 Spectral similarity produced by SID among the five AVIRIS data in Fig. 1.

	Blackbrush	Creosote	Drygrass	Redsoil	Sagebrush
Blackbrush	0	0.0497	0.0766	0.1861	0.0063
Creosote		0	0.2298	0.4154	0.0303
Drygrass			0	0.0640	0.0973
Redsoil				0	0.2340
Sagebrush					0

Table 4 Spectral similarity produced by HMMID among the five AVIRIS data in Fig. 1.

	Blackbrush	Creosote	Drygrass	Redsoil	Sagebrush
Blackbrush	0	1.5390	3.6717	3.9182	0.2263
Creosote		0	6.2549	6.7333	1.4102
Drygrass			0	1.1302	4.0073
Redsoil				0	3.4166
Sagebrush					0

Table 5 RSDPBs produced by ED, SAM, SID, and HMMID with \mathbf{t} chosen to be a mixture of 0.1055 blackbrush, 0.0292 creosote leaves, 0.0272 dry grass, 0.7588 red soil and 0.0974 sagebrush.

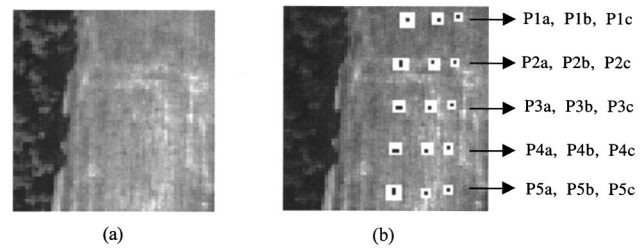
	Blackbrush	Creosote	Drygrass	Redsoil	Sagebrush
ED	0.2215	0.3417	0.1049	0.0773	0.2547
SAM	0.2212	0.3430	0.1044	0.0769	0.2546
SID	0.1897	0.4933	0.0588	0.0112	0.2500
HMMID	0.2395	0.4911	0.0511	0.0036	0.2147

Table 6 RSDEs of Table 5 produced by ED, SAM, SID, and HMMID.

	ED	SAM	SID	HMMID
RSDE	1.4835	1.4822	1.2274	1.1940

Table 7 RSDE of HMMID resulting from different numbers of states.

Number of States	3	4	5	6	7	8	9	10
RSDE	1.1940	1.1939	1.1938	1.1936	1.1932	1.1943	1.1941	1.1941

**Fig. 2** (a) HYDICE image scene that contains 15 panels and (b) spatial locations of 15 panels provided by ground truth.

pared to their counterparts produced by the ED, the SAM and the SID. However, inspecting the values in Tables 1–4, it may be difficult to compare the discriminatory power of the four measures.

To evaluate which measure is more effective in terms of spectral discriminability, a mixed spectral signature is randomly generated to be used as a target signature \mathbf{t} to be identified, which is composed of 0.1055 blackbrush, 0.0292 creosote leaves, 0.0272 dry grass, 0.7588 red soil and 0.0974 sagebrush. Note that the \mathbf{t} was generated randomly, not for a particular preference. From Tables 1–4, the spectrum of red soil is very similar to that of dry grass. Using Eq. (23) Table 5 tabulates the RSDPB of the ED, the SAM, the SID and the HMMID. The ratio of using the ED and the SAM to identify \mathbf{t} as red soil to identifying it as dry grass was $0.1049:0.0773 \approx 0.1044:0.0769 \approx 1.36$. Compared to the ED and the SAM, the SID and the HMMID yielded $0.0588:0.0112 \approx 5.25$ and $0.0511:0.0036 \approx 14.19$, respectively. This experiment shows that the HMMID was more effective than other three measures in identifying \mathbf{t} as red soil. Table 6 shows the RSDE of the ED, the SAM, the SID and the HMMID using Table 5 where the HMMID produced the least entropy. Table 7 tabulates the RSDE results of the HMMID using different numbers of states. We found that the RSDE decreased slightly as the number of states increased. However, a high number of states generally significantly increases the computational complexity of the parameter estimation process. Thus, according to our experiments, a reasonable number of states ranges from 4 to 6, which enables us to achieve a good compromise.

5.2 Example 2: HYDICE Data

Unlike the AVIRIS data studied in the previous section, the HYDICE data used in the following experiments were directly extracted from a HYDICE image scene of size 64×64 shown in Fig. 2(a), which has a large grass field on the right and a tree line on the left where low signal/high noise bands: bands 1 to 3 and bands 202 to 210; and water vapor absorption bands: bands 101 to 112 and bands 137 to 153 were removed. The spatial resolution is 1.5 m and spectral resolution is 10 nm. There are 15 panels located on the field and are arranged in a 5×3 matrix, as shown in Fig. 2(b).

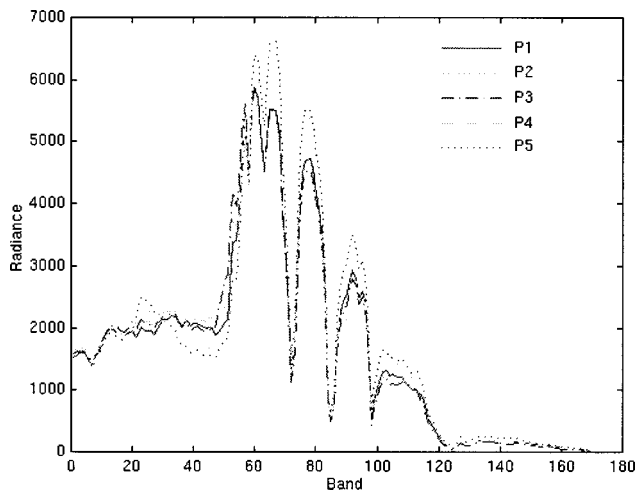


Fig. 3 Spectra of P_1 , P_2 , P_3 , P_4 and P_5 .

Each element in this matrix is a square panel and denoted by p_{ij} with row indexed by $i=1, \dots, 5$ and column indexed by $j=a, b, c$. For each row $i=1, \dots, 5$, the three panels p_{ia} , p_{ib} , p_{ic} were made by the same material but have three different sizes. For each column $j=a, b, c$, the five panels p_{1j} , p_{2j} , p_{3j} , p_{4j} , p_{5j} have the same size but were made by five different materials. Note that the panels in rows 2 and 3 are made by the same material with different paints, so did the panels in rows 4 and 5. Nevertheless, they were still considered as different materials. The sizes of the panels in the first, second and third columns are $3m \times 3m$, $2m \times 2m$ and $1m \times 1m$, respectively. Thus, the 15 panels have five different materials and three different sizes. The ground truth of the image scene provides the precise spatial locations of these 15 panels. As shown in Fig. 2(b), black pixels are the panel pixels and the pixels in the white masks are either panel boundary pixels mixed with background pixels or background pixels close to panels. The 1.5-m spatial resolution of the image scene suggests that all of these panels are only 1 pixel wide except that p_{2a} , p_{3a} , p_{4a} , p_{5a} which are 2-pixel panels. Figure 3 plots the five panel spectral signatures in Fig. 2(b), where the i 'th panel signature, denoted by P_i was obtained by averaging the black panel center pixels in row i . The spectra of P_1 , P_2 , P_3 , P_4 and P_5 were shown in Fig. 3 and formed the data set $\Delta = \{P_1, P_2, P_3, P_4, P_5\}$ that would be used for panel identification. Tables 8–11 tabulate the similarity values resulting from the ED, the SAM, the SID and the HMMID. Unlike Tables 1 and 2, the ED and the SAM generated different values in Tables 8 and 9. However, if the five panel signatures were normalized, the results produced by the ED and the SAM were close as shown in Tables 1 and 2. These two experiments showed that the ED and the SAM performed very similarly. From Tables 8–11, we can see that the signature of P_1 is close to that of P_2 , while P_2 is even closer to the signature of P_3 . Similarly, both P_4 and P_5 have very close signatures, which are very distinct from those of P_1 , P_2 and P_3 . This was confirmed by Fig. 4, which shows the detection results of the panels in each row using the constrained energy minimization (CEM) approach proposed in Ref. 11. The CEM-derived

Table 8 Spectral similarity produced by ED among the five HYDICE panel signatures in Fig. 3.

	P_1	P_2	P_3	P_4	P_5
P_1	0	1301.6	2033.3	4107.3	4831.6
P_2		0	1340.4	5064.1	5733.0
P_3			0	5434.1	5968.7
P_4				0	1125.4
P_5					0

Table 9 Spectral similarity produced by SAM among the five HYDICE panel signatures in Fig. 3.

	P_1	P_2	P_3	P_4	P_5
P_1	0	0.0435	0.0673	0.1144	0.1240
P_2		0	0.0430	0.1479	0.1567
P_3			0	0.1652	0.1710
P_4				0	0.0248
P_5					0

Table 10 Spectral similarity produced by SID among the five HYDICE panel signatures in Fig. 3.

	P_1	P_2	P_3	P_4	P_5
P_1	0	0.0039	0.0086	0.0233	0.0313
P_2		0	0.0033	0.0385	0.0484
P_3			0	0.0476	0.0570
P_4				0	0.0025
P_5					0

Table 11 Spectral similarity produced by HMMID among the five HYDICE panel signatures in Fig. 3.

	P_1	P_2	P_3	P_4	P_5
P_1	0	0.0255	0.0291	0.2935	0.4798
P_2		0	0.0215	0.2891	0.4483
P_3			0	0.3590	0.5483
P_4				0	0.0186
P_5					0

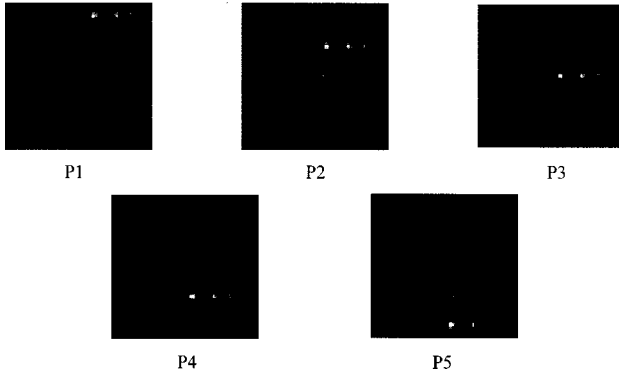


Fig. 4 Detection results of the 15 panels by CEM.

filter was developed based on the concept that it would pass the desired target \mathbf{t} through the filter while minimizing interfering effects resulting from sources other than the desired target \mathbf{t} . In doing so, it designs a finite impulse response (FIR) filter that constrains the desired target signature \mathbf{t} such as $P1$ to $P5$ in our experiments using a specific filter gain while minimizing the filter output energy caused by other signal sources including unknown interference. Its success in target detection for hyperspectral imagery has been demonstrated in Refs. 13–16. As we can see from Fig. 4, when panels in row 2 were detected, some panel pixels in row 3 were also detected as well and vice versa. Similarly, it was also true for panels in rows 4 and 5.

To see the performance of the proposed HMMID in terms of RSDPB, a target pixel randomly extracted from the white mask of p_{2c} was used as \mathbf{t} for identification since $P2$ is very close to both $P1$ and $P3$, but closer to $P3$. This pixel \mathbf{t} was a panel edge pixel mixed with the background grass signature. Table 12 shows the discriminatory probabilities against five panel signatures using the ED, the SAM, the SID and the HMMID. As we can see from Table 12, the RSDPBs among $P1$, $P2$ and $P3$ using the ED and the SAM were very close, and the HMMID was clearly the best. If we calculated the ratio of the second smallest RSDPB to the smallest RSDPB for the ED, SAM, SID and the HMMID, respectively,

$$p_{t,\Delta}^{\text{ED}}(P3):p_{t,\Delta}^{\text{ED}}(P2)=0.1530:0.1339\approx 1.14, \quad (25)$$

$$p_{t,\Delta}^{\text{SAM}}(P3):p_{t,\Delta}^{\text{SAM}}(P2)=0.1482:0.1108\approx 1.34, \quad (26)$$

$$p_{t,\Delta}^{\text{SID}}(P3):p_{t,\Delta}^{\text{SID}}(P2)=0.0813:0.0520\approx 1.56, \quad (27)$$

Table 12 RSDPBs produced by ED, SAM, SID, and HMMID with \mathbf{t} chosen from the white mask surrounding the panel of the second row and third column.

	$P1$	$P2$	$P3$	$P4$	$P5$
ED	0.1530	0.1339	0.1578	0.2631	0.2922
SAM	0.1544	0.1108	0.1482	0.2837	0.3028
SID	0.1029	0.0520	0.0813	0.3419	0.4218
HMMID	0.0994	0.0419	0.0939	0.3680	0.3968

Table 13 RSDPBs of Table 12 produced by ED, SAM, SID, and HMMID.

ED	SAM	SID	HMMID
1.5586	1.5344	1.3230	1.3190

$$p_{t,\Delta}^{\text{HMMID}}(P3):p_{t,\Delta}^{\text{HMMID}}(P2)=0.0939:0.0419\approx 2.24, \quad (28)$$

the HMMID was about twice as effective as the ED, the SAM, and SID to identify \mathbf{t} as $P2$. Table 13 tabulates their respective RSDPBs. Once again, the HMMID produced the least entropy.

6 Conclusion

This paper presents a new application of the HMM in hyperspectral image analysis. It uses the HMM to model the spectral properties of a hyperspectral pixel vector. A HMM-based hyperspectral measure, called HMMID is developed. One of the chief advantages of HMMID is that, as shown, success in speech recognition to capture sophisticated speech patterns, the HMM is also able to specify complicated hidden spectral properties that cannot be observed in the spectrum of pixel vectors. As the number of spectral channels grows, more subtle material substances will be extracted. These create more difficulty for spectral characterization. Under this circumstance, the HMMID has better ability than do ED, SAM and SID in characterizing spectral properties. This was demonstrated in the experiments. The disadvantage of HMMID is the complexity in the implementation of the HMM where the parameter triplet $\lambda = (\mathbf{A}, \mathbf{B}, \pi)$ used in the HMM must be estimated. However, this problem is not a major issue since the number of states required is generally small.

Acknowledgments

The authors would like to thank Bechtel Nevada Corporation under Contract No. DE-AC08-96NV11718 through the Department of Energy, Remote Sensing Laboratory, for their support and Dr. J. C. Harsanyi for providing the AVIRIS data. They also would like to thank an anonymous reviewer, whose comments significantly improved the presentation and quality of this paper.

References

1. G. Vane and A. F. H. Goetz, "Terrestrial imaging spectroscopy," *Remote Sens. Environ.* **24**, 1–29 (1988).
2. R. A. Schowengerdt, *Remote Sensing: Models and Methods for Image Processing*, 2nd ed., Academic Press (1997).
3. C.-I. Chang, "An information theoretic-based approach to spectral variability, similarity and discriminability for hyperspectral image analysis," *IEEE Trans. Inf. Theory* **46**, 1927–1932 (2000).
4. R. O. Duda and P. E. Hart, *Pattern Classification and Scene Analysis*, John Wiley & Sons, New York (1973).
5. L. Rabiner and B.-H. Juang, *Fundamentals of Speech Recognition*, Prentice-Hall, Englewood Cliffs, NJ (1993).
6. L. Rabiner and B.-H. Juang, "Introduction to hidden Markov models," *IEEE ASSP Mag.* 4–16 (1986).
7. L. Rabiner, "A tutorial on hidden Markov models and selected applications in speech recognition," *Proc. IEEE* **77**, 257–286 (1989).
8. C.-I. Chang and C. Brumbley, "A Kalman filtering approach to multispectral image classification and detection of changes in signature abundance," *IEEE Trans. Geosci. Remote Sens.* **37**, 257–268 (1999).
9. C.-I. Chang and C. Brumbley, "Linear unmixing Kalman filtering approach to signature abundance detection, signature estimation and

- subpixel classification for remotely sensed images," *IEEE Trans. Aerosp. Electron. Syst.* **37**, 319–330 (1999).
10. S. Kullback, *Information Theory and Statistics*, John Wiley & Sons, New York (1959), Dover (1968).
 11. J. C. Harsanyi, "Detection and classification of subpixel spectral signatures in hyperspectral image sequences," PhD Dissertation, Department of Electrical Engineering, University of Maryland Baltimore County (1993).
 12. J. Harsanyi and C.-I. Chang, "Hyperspectral image classification and dimensionality reduction: an orthogonal subspace projection approach," *IEEE Trans. Geosci. Remote Sens.* **32**, 779–785 (1994).
 13. J. C. Harsanyi, W. Farrand and C.-I. Chang, "Detection of subpixel spectral signatures in hyperspectral image sequences," in *Proc. Ann. Meeting, Am. Soc. Photogrammetry & Remote Sensing* pp. 236–247, Reno, NV (1994).
 14. W. Farrand, W. , and J. C. Harsanyi, "Mapping the distribution of mine tailing in the coeur d'Alene river valley, Idaho, through the use of constrained energy minimization technique," *Remote Sens. Environ.* **59**, 64–76 (1997).
 15. C.-I. Chang and D. Heinz, "Subpixel spectral detection for remotely sensed images," *IEEE Trans. Geosci. Remote Sens.* **38**, 1144–1159 (2000).
 16. H. Ren and C.-I. Chang, "Target-constrained interference-minimized approach to subpixel target detection for hyperspectral imagery," *Opt. Eng.* **39**, 3138–3145 (2000).



Qian Du received her PhD degree in electrical engineering from the University of Maryland, Baltimore County, in 2000. She is currently an assistant professor with the Department of Electrical Engineering and Computer Science, Texas A&M University-Kingsville. Dr. Du received her Dissertation Grant Award from the Phi Kappa Phi Chapter in the University of Maryland System in 2000. Her research interests include signal and image processing, pattern recognition,

data compression and neural networks. Dr. Du is a member of IEEE, SPIE and Phi Kappa Phi.



Chein-I Chang received his BS degree from Soochow University, Taipei, Taiwan, 1973, his MS degree from the Institute of Mathematics at National Tsing Hua University, Hsinchu, Taiwan, in 1975, and his MA degree from the State University of New York at Stony Brook, in 1977, all in mathematics. He also received MS and MSEE degrees from the University of Illinois at Urbana-Champaign in 1982 and his Ph.D. degree in electrical engineering from the

University of Maryland, College Park, in 1987. Dr. Chang has been with the University of Maryland Baltimore County (UMBC) since 1987, as a visiting assistant professor from January 1987 to August 1987, an assistant professor from 1987 to 1993, and an associate professor in the Department of Computer Science since 1993. He was a visiting research specialist with the Institute of Information Engineering at the National Cheng Kung University, Tainan, Taiwan, from 1994 to 1995. He holds a patent on automatic pattern recognition and has several pending patents on image processing techniques for hyperspectral imaging and detection of microcalcifications. He is currently on the editorial board of *Journal of High Speed Networks* and is the guest editor of a special issue of that journal on telemedicine and applications. His research interests include automatic target recognition, multispectral/hyperspectral image processing, medical imaging, documentation and text analysis, information theory and coding, signal detection and estimation, and neural networks. Dr. Chang is a senior member of IEEE and a member of SPIE, INNS, Phi Kappa Phi and Eta Kappa Nu.